PCCP

Accepted Manuscript




ROYAL SOCIETY OF CHEMISTRY

www.rsc.org/pccp

Cite this: DOI: 10.1039/c0xx00000x

www.rsc.org/xxxxxx

ARTICLE TYPE

# Exfoliated carbon nitride nanosheet decorated with NiS as efficient noble-metal-free visible-light-driven photocatalyst for hydrogen evolution

**Yongtao Lu,[a] Dongmei Chu,[a] Mingshan Zhu,[*b] Yukou Du[a] and Ping Yang[*a]**

***Received (in XXX, XXX) Xth XXXXXXXXX 20XX, Accepted Xth XXXXXXXXX 20XX***
**DOI: 10.1039/b000000x**

A binary composite composed of two dimensional (2D) ultrathin carbon nitride ($C_3N_4$) nanosheet and NiS nanoparticles was synthesized and applied as a noble-metal-free photocatalyst for hydrogen evolution under visible light irradiation. The ultrathin nanosheets of $C_3N_4$ were obtained by a facile liquid exfoliation method and used as 2D supports for the deposition of NiS nanoparticles. In the binary composite, the ultrathin $C_3N_4$ nanosheets acted as visible light responding semiconductor, and the NiS nanoparticles served as a noble-metal-free catalyst. The binary composite with optimized composition gave comparable hydrogen evolution rate to that of Pt modified $C_3N_4$. Moreover, compared to the bulk $C_3N_4$, the exfoliated $C_3N_4$ nanosheets distinctly improve the photocatalytic performance for hydrogen evolution. The photocatalytic results combined with photoelectrochemical experiments show that $C_3N_4$ with ultrathin structure promotes the electron-holes transportation and separation during the process of the photoinduced hydrogen evolution. This study displays a facile method to build a low-cost but effective photocatalyst for hydrogen production under visible light irradiation.

## 1. Introduction

Because of its high energy capacity and environmental friendliness, hydrogen has been thought as one of the most promising energy source compared with many other new energy carriers. Since the discovery of hydrogen evolution through the photoelectrochemical splitting of water on $TiO_2$ electrodes,[1] the technology of photocatalytic water splitting to produce hydrogen has been considering as an important approach to solve the world energy problem. Searching and optimizing efficient semiconductor-based photocatalysts for hydrogen production have attracted worldwide attentions. Recently, graphitic carbon nitride ($C_3N_4$) has emerged as a new class of photocatalyst due to its responsive to the visible light.[2-5] Scientists around the world use many strategies, such as dopping heteroatoms,[6-9] coupling with other semiconductors or dyes,[10-14] loading cocatalysts,[15-19] modification with carbon materials[20-23] and controlling morphology[25-28] to improve the catalytic activity of the $C_3N_4$-based catalysts. However, the most investigates focus on the bulk $C_3N_4$, which has small specific surface area with limited reactive sites and long diffusion length with high the recombination probability of photoexcited charges. More recently, researchers discovered ultrathin $C_3N_4$ nanosheets[29-32], which were prepared by thermal oxidation "etching" process, chemical exfoliation or sonication exfoliation, have large specific surface area, minimal thickness, and favorable bandgap. This kind of ultrathin $C_3N_4$ nanosheets displays evidently enhancement to photocatalytic activities compared with those of bulk $C_3N_4$.

As is well known, noble metal Pt nanoparticles have been widely used as cocatalyst for enhancing hydrogen evolution. However, the high cost and limited resources of this noble metal restricted the large scale application in the photocatalytic systems. From the view point of practical applications, the cocatalysts are required to be inexpensive, abundant and highly effective in photocatalytic hydrogen production. Recent studies have indicated that some transition metal sulfides or oxides including NiS,[17, 33] $MoS_2$,[34-36] $Ag_2O$,[37] $Cu_2O$,[38] $Ni(OH)_2$,[16,39] are economical and effective cocatalyst for improving $H_2$ production of the bulk $C_3N_4$. Accordingly, it is meaningful to develop hybrid materials by integrating $C_3N_4$ nanosheets and noble-metal free cocatalyst to achieve a higher efficiency for photocatalytic hydrogen production.

In this paper, we report a novel noble-metal-free photocatalyst composed of two dimensional (2D) ultrathin carbon nitride ($C_3N_4$) nanosheets and NiS nanoparticles (NiS NPs), which was fabricated through a hydrothermal method. The photocatalytic tests of the composite under visible light irradiation demonstrate that combining the exfoliated $C_3N_4$ nanosheets and NiS NPs remarkably improves the photocatalytic performance for hydrogen evolution. Considering the lower cost of NiS and superior photocatalytic performance of the binary composite, our studies would be impactful for developing noble metal free photocatalytic systems with high hydrogen generation efficiency.

## 2. Experimental Section

### 2.1. Materials

All chemicals were of analytical grade and purchased from Sinopharm Chemical Reagent Co., Ltd. without further purification before use.

### 2.2. Preparation of exfoliated graphitic carbon nitride (e-$C_3N_4$) nanosheets

The synthesis procedure of bulk $C_3N_4$ was according to the previous report with some modifications.[40] 10 g of ammonium thiocyanate was placed in quartz boat and heated at 823 K for 2 hours in Ar with a ramp rate of 5 °C $min^{-1}$. The obtained bulk $C_3N_4$ was grounded well into powders with a mortar. The as prepared samples were labeled as b-$C_3N_4$.

The graphitic carbon nitride nanosheets were fabricated by liquid exfoliation of bulk $C_3N_4$ powders as reported by Yang [30] with some modification (Scheme 1). In a typical fabrication, 300 mg bulk $C_3N_4$ were added into 250 mL flasks and then 100 mL isopropanol (IPA) was added into the above flasks as dispersion solvents. The sealed flasks were sonicated for 10 h. Then the supernatant was further centrifuged at 3000 rpm for 10 min and obtain the supernatant. After that, the isopropanol was evaporated on a rotary evaporator and the exfoliated $C_3N_4$ nanosheets were obtained. The as prepared samples were labeled as e-$C_3N_4$.

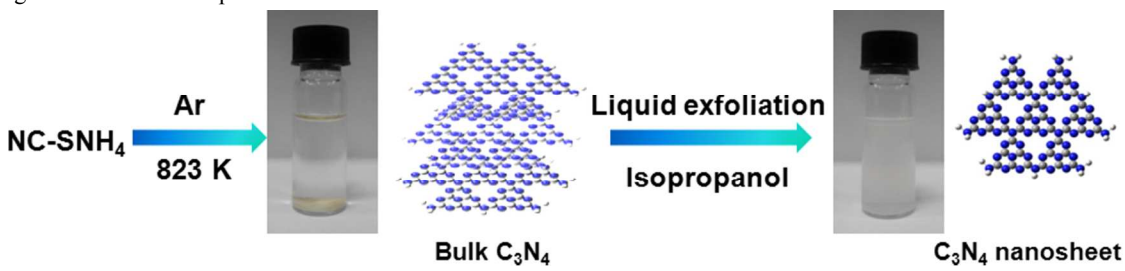


**Scheme 1** Scheme of the preparation process of exfoliated $C_3N_4$ nanosheets.

### 2.3. Preparation of exfoliated $C_3N_4$ nanosheets/NiS composite

The e-$C_3N_4$/NiS composite photocatalysts were prepared by the conventional precipitation and hydrothermal method. Typically, 150 mg as-prepared e-$C_3N_4$ nanosheets were dispersed in 20 mL $Ni(Ac)_2$ solution containing certain amount nickel acetate, and then 40 mL $Na_2S$ solution was added under the Ar atmosphere. The molar ratio of $Ni(Ac)_2/Na_2S$ was fixed at 1:3. The mixed solution was stirred at room temperature for 0.5 h. After that, the mixture was transferred to a 100 mL Teflon-lined autoclave and heated at 140 °C for 10 h. After being cooled to room temperature, the solid was isolated by centrifugation, washed with deionized water and ethanol for 3 times and dried in vacuum oven at 60°C. The as-prepared sample labeled as e-$C_3N_4$/NiS-x, where x stands for the weight percent of NiS of e-$C_3N_4$. For comparison, 1 wt% NiS hybridized with b-$C_3N_4$ was synthesized by similar method. Meanwhile, 1 wt% Pt loaded on the surface of the b-$C_3N_4$ was also synthesized using the in-situ photodeposition method.

### 2.4. Photoelectrochemical measurement

The photoelectrochemical experiment of the samples were measured using a CHI660D potentiostat/galvanostat electrochemical analyzer in a three-electrode system consisting of a working electrode, a platinum wire as a counter electrode, and a saturated calomel electrode (SCE) as a reference electrode. The working electrode was prepared by the drop-coating method. Indium tin oxide (ITO) conducting glass (1.0 cm*2.0 cm) was washed in water in an ultrasonic bath for 10 min, and then dried at room temperature. The sample (3 mg) was dispersed in (0.5 mL) ethylene glycol/ethanol solution in an ultrasonic bath for 30 min. The suspension was dropped onto the ITO glass and dried in a vacuum oven. The covered area of film was ca. 1.0 cm*1.5 cm. The electrodes were immersed in a supporting electrolyte solution of 0.1 M $Na_2SO_4$. The working electrode was irradiated with a GY-10 xenon lamp (150 W) during the measurement.

### 2.5. Photocatalytic reaction for hydrogen evolution

The photocatalytic reaction was carried out in a quartz flask equipped with a flat optical entry window. The effective irradiation area for the cell is ca. 3 $cm^2$. In a typical photocatalytic experiment, 50 mL of 10 vol% triethanolamine (TEOA) aqueous solution containing 50 mg of the fresh prepared catalyst were added into the quartz flask. Then the mixture was sonicated for 3 min at room temperature. The system was deaerated by bubbling argon into the solution for 30 min before light irradiating. A 150 W Xe lamp equipped with a cut-off filter at 400 nm was used as a visible light source. The lamp was positioned ca. 10 cm away from the optical entry window of the reactor. The produced hydrogen gas was analyzed with an online gas chromatograph equipped with a thermal conductivity detector (TCD) and 5 A molecular sieve columns using argon as carrier gas. The standard $H_2$/Ar gas mixtures of known concentrations were used for GC signal calibration. The apparent quantum efficiency (AQE) was measured under the same conditions except for replacing the 400 nm cut-off filter with a band pass interference filter centered at 420 nm.

### 2.6. Apparatus and measurements

Powder X-ray diffraction (XRD) patterns were recorded using an X-ray diffractometer (X' Pert-ProMPD) with Cu Kα irradiation (λ = 1.5406 Å). Fourier transform infrared (FT-IR) spectra of the samples were recorded on a Nicolet Magna 550 spectrometer. Transmission electron microscopy (TEM) studies were conducted using a transmission electron microscope (JEOL JEM-2100) operating at an accelerating voltage of 200 kV. Atomic force microscopy (AFM) images were recorded on a Digital Instrument Nanoscope IIIa Multimode system (Santa Barbara, CA) with a silicon cantilever using tapping mode. The sample for AFM measurement was prepared by spraying the diluted suspension of $C_3N_4$ nanosheet onto a silicon wafer and dried in air. The ultraviolet-visible diffuse reflectance spectra (DRS) were

obtained using a UV-visible spectrophotometer (Shimadzu UV-3150). The metal compositions in the photocatalysts were measured using inductively coupled plasma (ICP) optical emission spectrometer (Varian 710-ES).

## 3. Results and discussion

### 3.1 Characterization of the photocatalysts

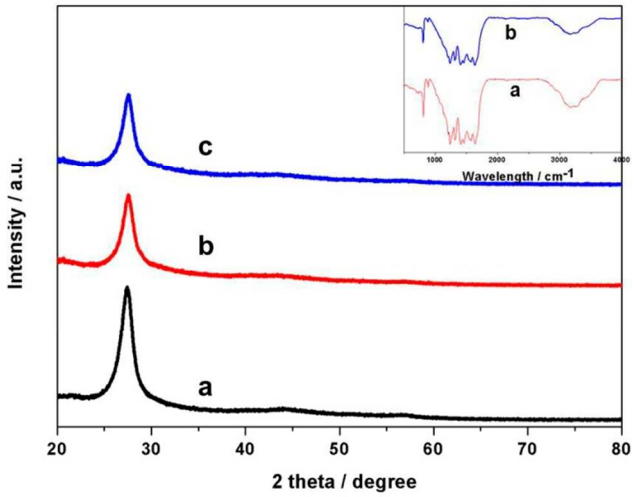


**Fig. 1** XRD patterns of (a) b-$C_3N_4$, (b) e-$C_3N_4$ and (c) e-$C_3N_4$/NiS. The inset shows FTIR spectra of (a) b-$C_3N_4$ and (b) e-$C_3N_4$.

The ultrathin e-$C_3N_4$ nanosheets were fabricated by liquid exfoliation of b-$C_3N_4$ powders. The XRD patterns of e-$C_3N_4$ and e-$C_3N_4$/NiS are presented in Fig. 1. For comparison, the XRD pattern of b-$C_3N_4$ is also presented. In the case of b-$C_3N_4$, the strong XRD peak at 27.7°, indexed as (002) reflection of the graphitic system, is a characteristic interlayer stacking reflection of b-$C_3N_4$. After exfoliation, the intensity of this (002) peak significantly decreases, which clearly demonstrates that the layered $C_3N_4$ has been successfully procured.[30] For the e-$C_3N_4$/NiS sample, the diffraction peak located at ca. 27.7°is the same as that of the e-$C_3N_4$ nanosheets, demonstrating the presence of e-$C_3N_4$ in the composite. No diffraction peaks can be attributed to the NiS NPs, which might be due to the low content (1 wt %) and high dispersion of the component. The mass percentage of NiS was determined by ICP analysis and the results show that the actual NiS contents in the e-$C_3N_4$/NiS are 0.97%, 1.82% and 2.69%, for e-$C_3N_4$/NiS-1.0, e-$C_3N_4$/NiS-2.0 and e-$C_3N_4$/NiS-3.0 samples, respectively.

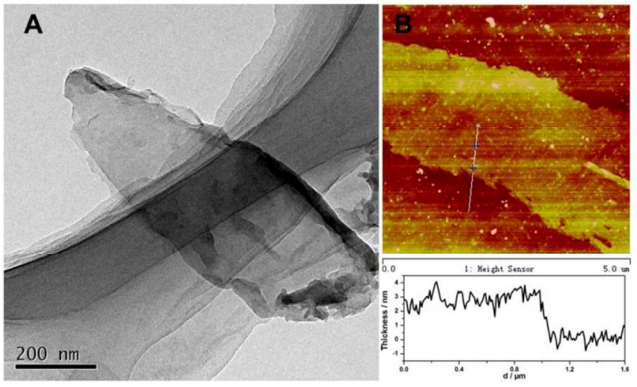


**Fig. 2** (A) The TEM image of e-$C_3N_4$ nanosheets and (B) the tapping-mode AFM image of a $C_3N_4$ nanosheet deposited on the silicon substrate and corresponding thickness analysis taken around the white line in AFM image.

The inset of Fig. 1 presents the FTIR spectra of b-$C_3N_4$ and e-$C_3N_4$. Basically, the spectra of the both samples are similar, indicating that e-$C_3N_4$ has the same chemical structure as b-$C_3N_4$. The peak at 810 $cm^{-1}$ is characteristic breathing mode of the triazine units of $C_3N_4$. The set of peaks between about 1881 and 909 $cm^{-1}$ is characteristic vibrations of s-triazine derivatives. The broad band between 3670 and 2785 $cm^{-1}$ is originated from the N–H stretches, suggesting the partial hydrogenation of some nitrogen atoms in $C_3N_4$.[30, 31]

The morphology of as-prepared samples was investigated via TEM and AFM. The TEM image (Fig. 2A) illustrates the very transparent feature of e-$C_3N_4$, indicating formation of few-layer $C_3N_4$. Fig. 2B shows the typical AFM image of the e-$C_3N_4$ nanosheet. The thickness analysis of the nanosheet by AFM reveals an average thickness of about 3.4 nm, which is in accordance with the transparent feature of the nanosheet obtained from TEM image. These evidences clearly demonstrated that b-$C_3N_4$ has been successfully exfoliated into ultrathin $C_3N_4$ nanosheets. The TEM image of e-$C_3N_4$/NiS was shown in Fig. 3A. From the image, the intimate contact between the NiS NPs and e-$C_3N_4$ is clearly observed, which could improve the charge separation of e-$C_3N_4$ and therefore the photocatalytic activity. The HRTEM image (Fig. 3B) of NiS in the composite shows a lattice plane with spacing of 0.201 nm, corresponding to (102) plane of NiS.[17] It indicated sufficiently that NiS nanoparticles were loaded on e-$C_3N_4$ nanosheets successfully.

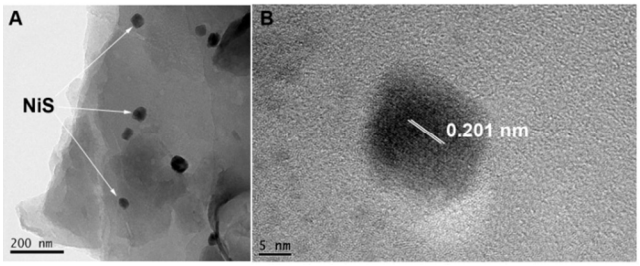


**Fig. 3** (A) The TEM image of e-$C_3N_4$/NiS. (B) The HRTEM image of NiS nanoparticle.

### 3.2 Optical and photoelectrochemical properties

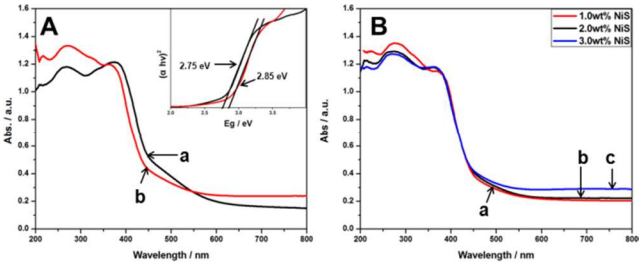


**Fig. 4** (A) DRS spectra of the b-$C_3N_4$ (a) and e-$C_3N_4$ (b). (B) DRS spectra of e-$C_3N_4$/NiS-1.0 (a), e-$C_3N_4$/NiS-2.0 (b), e-$C_3N_4$/NiS-3.0 (c).

The optical properties of the as-prepared smples have been investigated by UV-Vis diffuse reflectance spectra (DRS), as shown in Fig. 4A. It is found that the absorption edge of e-$C_3N_4$ shows a remarkable blue shift compared with that of b-$C_3N_4$,

corresponding to an increase in the band gap from 2.75 eV to 2.85 eV (inset of Fig. 4A). The blue shift performance is attributed to the quantum confinement effect by shifting the band edges of the conduction band and valence band in opposite directions.[31] Fig.4B shows the DRS spectra of different loading amounts of the e-$C_3N_4$/NiS samples. Compared with e-$C_3N_4$, the UV-vis DRS spectra of e-$C_3N_4$/NiS samples indicate that combining NiS with e-$C_3N_4$ does not cause any obvious the absorption edge shift. The absorption intensity in the visible region increases as the amount of NiS in the nanocomposite augments, which can be ascribed to the absorption of NiS in the range of 300–800 nm.[17]

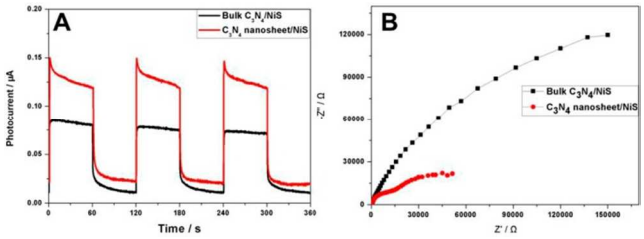


**Fig. 5** (A) Photocurrent responses of b-$C_3N_4$/NiS and e-$C_3N_4$/NiS to light irradiation recorded at 0.2 V vs. SCE. The electrolyte was 0.1 M $Na_2SO_4$ aqueous solution. The illumination from a 150 W xenon lamp was interrupted every 60 s. (B) Nyquist plots of electrochemical impedance spectra (EIS) for b-$C_3N_4$/NiS and e-$C_3N_4$/NiS in 0.1 M $Na_2SO_4$ aqueous solution.

The improved charge carrier separation in ultrathin $C_3N_4$ nanosheet is investigated by the photocurrent experiments and electrochemical impedance spectra. As shown in Fig. 5A, fast and reversible photocurrent responses can be observed for both b-$C_3N_4$/NiS and e-$C_3N_4$/NiS electrode. However, the e- $C_3N_4$/NiS electrode demonstrates higher photocurrent density than that of b-$C_3N_4$/NiS. The photocurrent of the e-$C_3N_4$/NiS electrode is about 2 times as high as that of b-$C_3N_4$/NiS. The electrochemical impedance spectra (EIS) presented as Nyquist plots of the b-$C_3N_4$/NiS and e-$C_3N_4$/NiS electrodes are shown in Fig. 5B. The e-$C_3N_4$/NiS electrode shows a smaller diameter compared with that of b-$C_3N_4$/NiS, indicating a decrease of resistance and the improvement in charge transfer at the interface of the e-$C_3N_4$/NiS electrode/electrolyte. These facts demonstrate that the e-$C_3N_4$ nanosheets in the nanocomposite may significantly improve the conductivity of the electrode, which in turn enhances the separation efficiency of photo induced electrons and holes.[41]

The flat band potentials ($E_{fb}$) of the nanocomposites were determined by the onset potential of the Mott–Schottky plots. [42] As shown in the Fig. 6A and 6B, the positive slopes of the linear plot suggest n-type semiconductor features of both e-$C_3N_4$ and b-$C_3N_4$. The value of $E_{fb}$ for the b-$C_3N_4$ electrode estimated from the x intercepts of the linear region of the Mott–Schottky plot is ca. −1.32 V vs. SCE, while it is ca. −1.22 V vs. SCE for the e-$C_3N_4$ electrode. These results shows that both b-$C_3N_4$ and e-$C_3N_4$ thermodynamically enables photocatalytic reduction of water ($H^+/H_2$: -0.41 V vs SHE at pH=7) even though the flat-band potential of e-$C_3N_4$ is more positive than that of b-$C_3N_4$.The results of the linear sweep voltammetry investigating the hydrogen evolution potential are shown in Fig. 6C. For the b-$C_3N_4$/NiS electrode, the proton reduction potential is ca. −1.07 V vs. SCE, while for the e-$C_3N_4$/NiS electrode the value changes to −0.99 V vs. SCE, demonstrating that hydrogen gas evolved more easily from the e-$C_3N_4$/NiS electrode than from b-$C_3N_4$/NiS.

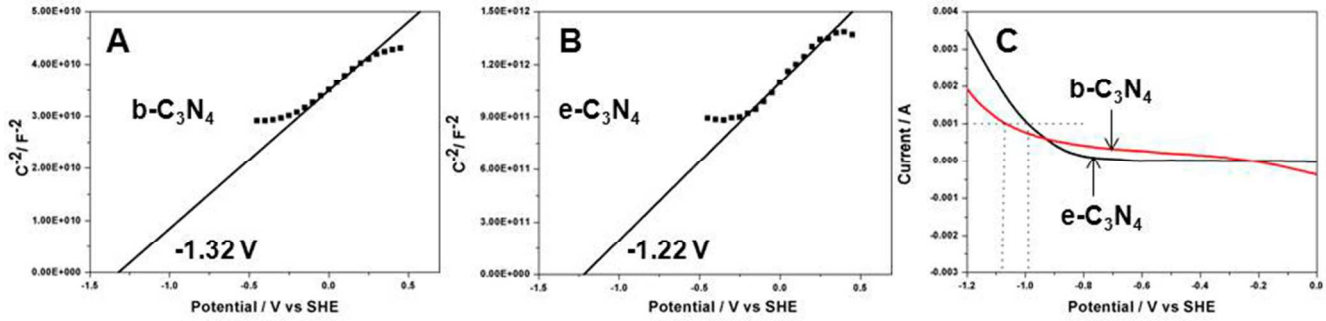


**Fig. 6** The Mott–Schottky plot of the b-$C_3N_4$ (A) and e-$C_3N_4$ (B) sample. (C) The liner sweep voltammetry of b-$C_3N_4$/NiS-1.0 and e-$C_3N_4$/NiS-1.0 electrodes in 0.10 mol $L^{-1}$ $Na_2SO_4$. Hydrogen evolution potential determined at 0.001 A is −1.07 V for b-$C_3N_4$/NiS-1.0 and −0.99 V for e-$C_3N_4$/NiS-1.0.

### 3.3 Photoinduced hydrogen evolution

Photocatalytic $H_2$ production activities of the as-prepared samples under visible light irradiation (λ>400 nm) using triethanolamine as an electron donor are shown in Fig. 7A. It is found that the e-$C_3N_4$/NiS-1.0 catalyst shows superior photocatalytic activity to b-$C_3N_4$/NiS-1.0. The rate of $H_2$ evolution over e-$C_3N_4$/NiS reaches 4.2 μmol $h^{-1}$, which is about *ca.* 2.6 times as high as that of b-$C_3N_4$/NiS (1.6 μmol $h^{-1}$). Similar results were also obtained for the Pt loaded $C_3N_4$ samples. The rate of $H_2$ evolution over b-$C_3N_4$/Pt is ca. 2.2 μmol $h^{-1}$ and the rate of $H_2$ evolution over e-$C_3N_4$/Pt is ca. 5.6 μmol $h^{-1}$. The fact that e-$C_3N_4$ remarkably enhances photocatalytic activity can be explained as the effects of large surface area and improved electron transport ability of e-$C_3N_4$. Due to the small sheet thickness around 3 nm of e-$C_3N_4$, electron transport ability improved and the bulk recombination probability of charge carriers substantially reduced in the e-$C_3N_4$/NiS catalyst, which certainly improve photocatalytic activities of e-$C_3N_4$-based catalyst. Though photocatalytic activity of e-$C_3N_4$/Pt is a little higher than that of the e-$C_3N_4$/NiS samples, consideration high cost of Pt, combining NiS with e-$C_3N_4$ nanosheets can be an efficient way for fabricating effective catalyst for the photocatalytic hydrogen production. NiS was deposited on the e-$C_3N_4$ and has imitated contact with e-$C_3N_4$. NiS provide the reaction site for the hydrogen production and it can reduce the over potential of hydrogen production. Fig. 7B shows the influence of the amount of NiS in the nanocomposite on the photocatalytic activity of e-$C_3N_4$/NiS photocatalysts. No $H_2$ can

be detected using NiS nanoparticles (NPs) as the photocatalyst, suggesting that NiS itself was not active for photocatalytic $H_2$ evolution. Pure e-$C_3N_4$ nanosheets only show a negligible photocatalytic activity (ca. 0.2 μmol $h^{-1}$). Combining NiS with the e-$C_3N_4$ nanosheets leads to a hydrogen production enhancement compared to the bare e-$C_3N_4$ nanosheets. When 1 wt% NiS was loaded on the e-$C_3N_4$ nanosheets composite, the total amount of hydrogen evolved over the composite is 42.3 μmol under 10 h visible-light irradiation. However higher loading of NiS decreases the photocatalytic activity of the composite catalyst, which may be attributed to the following two factors: (i) high loading content of NiS leads to a decrease in the surface active sites of e-$C_3N_4$ nanosheets; (ii) excess NiS NPs covered on the surface of $C_3N_4$ nanosheets may shield the incident light, thus preventing the generation of electrons.

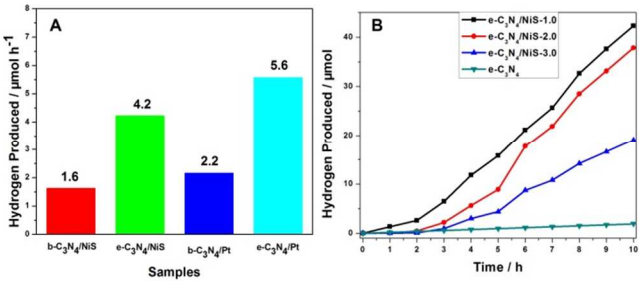


**Fig. 7** (A) Photocatalytic hydrogen production on b-$C_3N_4$/NiS-1.0, e-$C_3N_4$/NiS-1.0, b-$C_3N_4$/Pt-1.0 and e-$C_3N_4$/Pt-1.0. (B) Influence of the NiS content on the photocatalytic activity of e-$C_3N_4$ and e-$C_3N_4$/NiS. Reaction conditions: 50 mg photocatalysts, 45 mL $H_2O$, 5 mL TEOA, in Ar atmosphere, 150 W Xe lamp equipped with a cut-off filter at 400 nm.

Fig. 8 shows photocatalytic hydrogen production rate with different wavelengths and the DRS of the sample e-$C_3N_4$/NiS-1.0. The $H_2$ evolution rate was 1.3 μmol $h^{-1}$ when a 365 nm band pass filter was used. In the visible region, the $H_2$ evolution rates were 0.9, 0.7 and 0.2 μmol $h^{-1}$ when 420 nm, 460 nm and 505 nm band pass filter were used and the AQE is 1.4% at 420 nm. The trend of the hydrogen production rate matches well with the optical absorption spectrum. It clearly illustrates that the light absorption indeed induces the photocatalytic production of $H_2$. We also compare our result with some other groups' work. The photocatalytic activity of our system is lower than their results[16, 32, 33] since the lamp output power (150 W) is lower than that of other group. But the apparent quantum efficiency is comparable with others.

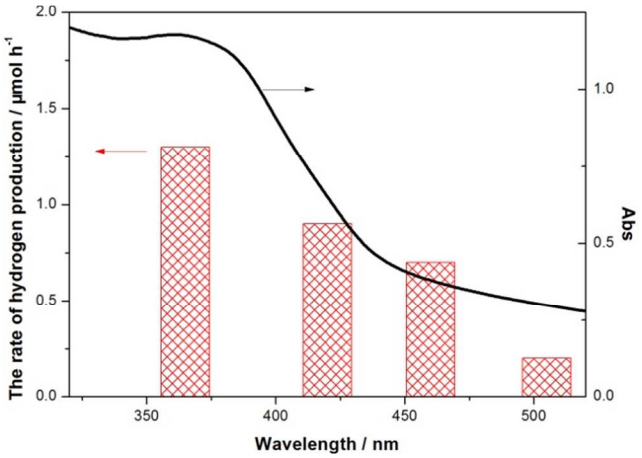


**Fig. 8** Dependences of photocatalytic hydrogen production rate on the wavelengths and DRS of the sample e-$C_3N_4$/NiS-1.0.

The photocatalytic stability of e-$C_3N_4$/NiS-1.0 was investigated by cycle photocatalytic experiments and the results are shown in Fig. 9. Under visible light irradiation, e-$C_3N_4$/NiS-1.0 produced 42.3 μmol $H_2$ in the first run after 10 h light irradiation. In the following two runs, the amount of hydrogen evolved from the system is 39.0 and 38.1 μmol. Furthermore, the recovered photocatalyst was characterized by TEM and XRD techniques (Fig. S1 and S2). The TEM image shows that the NiS nanoparticles were deposited on the $C_3N_4$ nanosheets as the original sample. And the XRD pattern of the e-$C_3N_4$/NiS-1.0 after the photocatalytic reaction is nearly the same as that of e-$C_3N_4$/NiS-1.0 before the photocatalytic reaction. These results suggest that e-$C_3N_4$/NiS-1.0 is a stable photocatalyst under visible light irradiation.

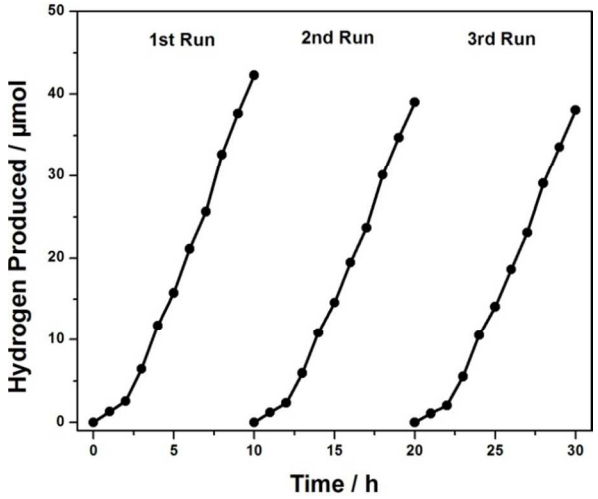


**Fig. 9** The recycling experiment of e-$C_3N_4$/NiS-1.0. Reaction conditions: 50 mg photocatalysts, 45 mL $H_2O$, 5 mL TEOA, 150 W Xe lamp equipped with a cut-off filter at 400 nm.

Based on the experiment results, a possible mechanism for visible light induced hydrogen production on the nanocomposite is illustrated as follows: Firstly, the e-$C_3N_4$ nanosheets absorb photons of higher energies than required than the band gap to produce the electron-hole pair and the electrons are excited to the conduction band. Secondly, electrons migrated to the surface while they may recombine each other on their transfer. In this

step, electrons in the exfoliated $C_3N_4$ nanosheets transfer more efficiently than that of bulk $C_3N_4$ due to its morphology. It is beneficial for the photocatalytic hydrogen production. Thirdly the $H^+$ ions accept the electrons from the NiS nanoparticles to produce the hydrogen while the electrons in the surface of $C_3N_4$ do not react with the $H^+$ ions. Future more NiS can reduce the over potential of hydrogen production. Finally, the TEOA was oxidized to its oxidation product.

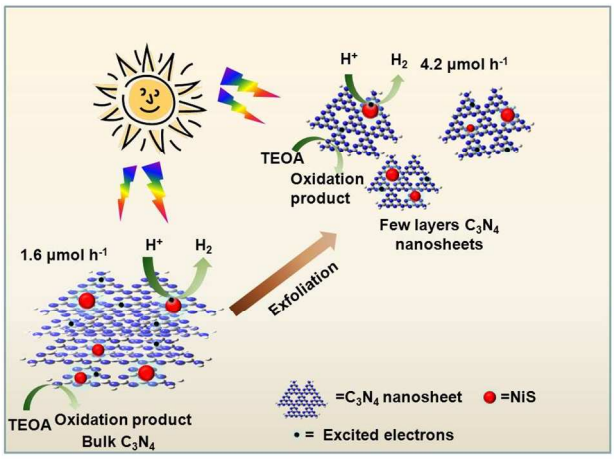


**Scheme 2** Schematic illustration of the visible light photocatalytic performance of the NiS loaded e-$C_3N_4$ nanosheets and b-$C_3N_4$.

## Conclusions

A novel nanocomposite composed of e-$C_3N_4$ and NiS NPs as a photocatalyst has been synthesized. NiS NPs are well anchored on the two dimensional e-$C_3N_4$ sheets of the nanocomposite, resulting in the excellent interfacial contact between e-$C_3N_4$ and NiS NPs. In comparison of b-$C_3N_4$, the binary composite with the optimal composition showed good photocatalytic performance and superior stability for $H_2$ evolution with visible light illumination. This is because compared with the b-$C_3N_4$, the ultrathin $C_3N_4$ nanosheets efficiently promotes the electron–hole separation, lengthens the charge lifetimes in the process of photocatalytic reaction. Considering the lower cost of NiS compared with noble metal and superior electronic features of ultrathin e-$C_3N_4$ nanosheets, this study exhibits a facile method to build a low-cost but effective photocatalyst for hydrogen production under visible light illumination.

### Acknowledgements

The authors are grateful for the financial support of this research by the National Natural Science Foundation of China (21373143) and the Priority Academic Program Development of Jiangsu Higher Education Institutions (PAPD).

## Notes and references

[a] *College of Chemistry, Chemical Engineering and Materials Science, Soochow University, Suzhou 215123, P.R. China. Fax: +86 512 65880089; Tel: +86 512 65880361; E–mail: pyang@suda.edu.cn (P. Yang)*

[b] *Department Chemistry and Impact Centre, University of Toronto, Toronto M5S 3H6, Canada. E-mail:mingshanzhu@yahoo.com, mingshanzhu@utoronto.ca (M. Zhu)*

1 K. Fujishima, A. Honda, *Nature*, 1972, **238,** 37-38.
2 X. Wang, K. Maeda, A. Thomas, K. Tgakanabe, G. Xin, J. M. Carlsson, K. Domen and M. Antonietti, *Nat. Mater.*, 2009, **8,** 76-80.
3 S. Cao and J. Yu, *J. Phys. Chem. Lett.*, 2014, **5,** 2101-2107.
4 Y. Wang, X. Wang and M. Antonietti, *Angew. Chem., Int. Ed.*, 2012, **51,** 68-89.
5 X. Wang, S. Blechert and M. Antonietti, *ACS Catal.*, 2012, **2,** 1596-1606.
6 Z. Lin and X. Wang, *Angew. Chem., Int. Ed.*, 2013, **52,** 1735-1738.
7 J. Hong, X. Xia, Y. Wang, R. Xu, *J. Mater. Chem.*, 2012, **22,** 15006-15012.
8 J. Li, B. Shen, Z. Hong, B. Lin, B. Gao and Y. Chen, *Chem. Commun.*, 2012, **48,** 12017-12019.
9 G. Liu, P. Niu, C. Sun, S. C. Smith, Z. Chen, G. Q. Lu and H. Cheng, *J. Am. Chem. Soc.*, 2010, **132,** 11642-11648.
10 S. Cao, X. Liu, Y. Yuan, Z. Zhang, Y. Liao, J. Fang, S. C. J. Loo, T. C. Sum and C. Xue, *Appl. Catal. B* 2014, **147,** 940-946.
11 J. Fu, B. Chang, Y. Tian, F. Xi and X. Dong, *J. Mater. Chem. A*, 2013, **1,** 3083-3090.
12 X. Zhang, L. Yu, C. Zhuang, T. Peng, R. Li and X. Li, *ACS Catal*,. 2013, **4,** 162-170.
13 Y. Wang, J. Hong, W. Zhang, R. Xu, *Catal. Sci. Technol.*, 2013, **3,** 1703-1711.
14 S. Cao, X. Liu, Y. Yuan, Z. Zhang, J. Fang, S. C. J. Loo, J. Barber, T. C. Sum and C. Xue, *Phys. Chem. Chem. Phys.*, 2013, **15,** 18363-18366.
15 S. Samanta, S. Martha and K. Parida, *ChemCatChem,* 2014, **6,** 1453-1462.
16 J. Yu, S. Wang, B. Cheng, Z. Lin, F. Huang, *Catal. Sci. Technol.*, 2013, **3,** 1782-1789.
17 Z. Chen, P. Sun, B. Fan, Z. Zhang and X. Fang, *J. Phys. Chem. C*, 2014, **118,** 7801-7807.
18 L. Yin, Y. Yuan, S. Cao, Z. Zhang and C. Xue, *RSC Adv.*, 2014, **4,** 6127-6132.
19 L. Ge, C. Han, J. Liu and Y. Li, *Appl. Catal. A*, 2011, **409-410,** 215-222.
20 Q. Xiang, J. Yu and M. Jaroniec, *J. Phys. Chem. C*, 2011, **115,** 7355-7363.
21 L. Ge and C. Han, *Appl. Catal. B* 2012, **117-118,** 268-274.
22 Z. Wu, H. Gao, S. Yan and Z. Zou, *Dalton Trans.*, 2014, **43,** 12013-12017.
23 L. Shi, L. Liang, J. Ma, F. Wang and J. Sun, *Dalton Trans.*, 2014, **43,** 7236-7244.
24 H. Yan, *Chem. Commun.*, 2012, **48,** 3430-3432.
25 X. Chen, Y. Jun, K. Takanabe, K. Maeda, K. Domen, X. Fu, M. Antonietti and X. Wang, *Chem. Mater.*, 2009, **21,** 4093-4095.
26 K. Kailasam, J. D. Epping, A. Thomas, S. Losse and H. Junge, *Energy Environ. Sci.*, 2011, **4,** 4668-4674.
27 J. Liu, J. Huang, H. Zhou and M. Antonietti, *ACS Appl. Mater. Interfaces*, 2014, **6,** 8434-8440.
28 X. Wang, K. Maeda, X. Chen, K. Takanabe, K. Domen, Y. Hou, X. Fu and M. Antonietti, *J. Am. Chem. Soc.*, 2009, **131,** 1680-1681.
29 P. Niu, L. Zhang, G. Liu and H. Cheng, *Adv. Funct. Mater.*, 2012, **22,** 4763-4770.

30 S. Yang, Y. Gong, J. Zhang, L. Zhan, L. Ma, Z. Fang, R. Vajtai, X. Wang and P. M. Ajayan, *Adv. Mater.*, 2013, **25,** 2452-2456.

31 J. Xu, L. Zhang, R. Shi and Y. Zhu, *J. Mater. Chem. A*, 2013, **1,** 14766-14772.

32 K. Schwinghammer, M. B. Mesch, V. Duppel, C. Ziegler, J. Senker and B. V. Lotsch, *J. Am. Chem. Soc.*, 2014, **136,** 1730-1733.

33 J. Hong, Y. Wang, Y. Wang, W. Zhang and R. Xu, *ChemSusChem*, 2013, **6,** 2263-2268.

34 L. Ge, C. Han, X. Xiao and L. Guo, *Int. J. Hydrogen Energy*, 2013, **38,** 6960-6969.

35 Y. Hou, A. B. Laursen, J. Zhang, G. Zhang, Y. Zhu, X. Wang, S. Dahl and I. Chorkendorff, *Angew. Chem. Int. Ed.*, 2013, **52,** 3621-3625.

36 J. Wang, Z. Guan, J. Huang, Q. Li and J. Yang, *J. Mater. Chem. A*, 2014, **2,** 7960-7966.

37 L. Shi, L. Liang, J. Ma, F. Wang and J. Sun, *Catal. Sci. Technol.*, 2014, **4,** 758-765.

38 J. Chen, S. Shen, P. Guo, M. Wang, P. Wu, X. Wang and L. Guo, *Appl. Catal. B* 2014, **152-153**, 335-341.

39 Z. Yan, X. Yu, A. Han, P. Xu, and P. Du, *J. Phys. Chem. C*, 2014, **118,** 22896-22903.

40 Y. Cui, J. Zhang, G. Zhang, J. Huang, P. Liu, M. Antonietti and X. Wang, *J. Mater. Chem.* 2011, **21,** 13032-13039.

41 Z. Mou, S. Yin, M. Zhu, Y. Du, X. Wang, P. Yang, J. Zheng, C. Lu. *Phys. Chem. Chem. Phys*. 2013, **15,** 2793-2799.

42 F. Cardon and W. P. Gomes, *J. Phys. D: Appl. Phys.*, 1978, **11,** L63.